Original Research Paper

Reversing ferroptosis resistance by MOFs through regulation intracellular redox homeostasis

Chengcheng Wang[a], Jiao Wang[b], Xue Pan[c], Shuang Yu[a], Meiqi Chen[a], Yan Gao[a], Zilin Song[a], Haiyang Hu[a], Xiuli Zhao[a], Dawei Chen[a], Fei Han[a],*, Mingxi Qiao[a],*

[a] *School of Pharmacy, Shenyang Pharmaceutical University, Shenyang 110016, China*
[b] *Yantai Luyin Pharmaceutical Co. Ltd., Yantai 264002, China*
[c] *Qingdao Marine Biomedical Research Institute, Qingdao 266071, China*

ARTICLE INFO

ABSTRACT

As a non-apoptotic cell death form, ferroptosis offers an alternative approach to overcome cancer chemotherapy resistance. However, accumulating evidence indicates cancer cells can develop ferroptosis resistance by evolving antioxidative defense mechanisms. To address this issue, we prepared a Buthionine-(S,R)-sulfoximine (BSO) loaded metal organic framework (MOF) of BSO-MOF-HA (BMH) with the combination effect of boosting oxidative damage and inhibiting antioxidative defense. MOF nanoparticle was constructed by the photosensitizer of [4,4,4,4-(porphine-5,10,15,20-tetrayl) tetrakis (benzoic acid)] (TCPP) and the metal ion of Zr6, which was further decorated with hyaluronic acid (HA) in order to impart active targeting to CD44 receptors overexpressed cancer cells. BMH exhibited a negative charge and spherical shape with average particle size about 162.5 nm. BMH was found to restore the susceptibility of 4T1 cells to ferroptosis under irradiation. This was attributed to the combination of photodynamic therapy (PDT) and γ-glutamylcysteine synthetase inhibitor of BSO, shifting the redox balance to oxidative stress. Enhanced ferroptosis also induced the release of damage associated molecular patterns (DAMPs) to maturate dendritic cells and activated T lymphocytes, leading to superior anti-tumor performance *in vivo*. Taken together, our findings demonstrated that boosting oxidative damage with photosensitizer serves as an effective strategy to reverse ferroptosis resistance.

© 2022 Shenyang Pharmaceutical University. Published by Elsevier B.V. This is an open access article under the CC BY-NC-ND license (http://creativecommons.org/licenses/by-nc-nd/4.0/)

1. Introduction

Recently, a distinct form of regulated cell death of ferroptosis has attracted intensive attention [1–3]. This type of cell death relies on overwhelming reactive oxygen species (ROS) production which is induced by reduced glutathione (GSH) level and glutathione peroxidase 4 (GPX4) activity or the excessive iron accumulation to boost Fenton reaction $(Fe^{2+} + H_2O_2 = Fe^{3+} + (OH)^- + \bullet OH)$ [4–7]. According to the ROS production mechanism, ferroptosis inducers (FINs) could be divided into three types [8–11]: (1) class I FINs tended

to inhibit GSH synthesis, such as erastin and glutamate. (2) class II FINs directly inactivated GPX4, such as RSL3 and FIN56, and (3) iron loaded nanoparticles tended to boost Fenton reaction, such as Fe_3O_4 and ferric ammonium citrate [12,13]. Because apoptosis based cancer treatment are facing severe challenges of multi-drug resistance, ferroptosis certainly provides an alternative approach to eradicate tumor cells [14]. Moreover, ferroptotic cancer cells were also able to activate antitumor immune response through triggering immunogenic cell death (ICD) effect [15–17]. Cancer cells undergoing ICD could release damage-associated molecular patterns (DAMPs) such as adenosine triphosphate (ATP), high mobility group box 1 (HMGB1) and calreticulin (CRT) and to maturate DCs and subsequently activate cytotoxicity T lymphocytes [18–20]. Afterwards, activated CD4$^+$ and CD8$^+$ T lymphocytes would directly eradicate malignant tumor cells and thereby reinforce the anti-tumor immune response *in vivo* [21–23]. Collectively, ferroptosis is a promising cancer treatment owing to the success in overcoming multidrug resistance and activating the systemic immune response.

Despite the potential of ferroptosis, different response to ferroptosis stress have been observed across multiple cancer cell lines. Effective ferroptosis is only observed in about 30% of cancer cells which express mutated small GTPases or P53 expression [24]. Meanwhile, it is worth to note that some cancer cells were able to evolve antioxidant defensive mechanisms such as enhanced antioxidant systems, dysregulated iron and lipid metabolisms, leading to ferroptosis resistance. For example, cancer cells with activated nuclear factor erythroid 2-related factor 2 (Nrf2) pathway demonstrated ferroptosis resistance to class I FINs [25,26]. Cancer cells with highly expressed and stabilized system Xc- (a cystine/glutamate antiporter) were found to accelerate GSH synthesis to diminish excessive ROS [27,28]. The system Xc- also combine thioredoxin (TXN) to rescue GSH deficiency [29,30]. Iron related genes were also unregulated to export excess iron ions and pyruvate dehydrogenase kinase 4 (PDK4) inhibited fatty acid synthesis and subsequently blocked the fuels for lipid peroxidation in ferroptosis [31,32].

Considering the fact that ferroptosis is an iron and lipid peroxidation dependent lethal modality, the regulation between intracellular oxidative damage and antioxidant defense is the key for ferroptosis susceptibility. Therefore, the combination of boosting oxidative damage and inhibiting antioxidative defense would be an effective approach to address the ferroptosis resistance. Nowadays, photodynamic therapy (PDT) is emerging as a promising approach in cancer treatment because of the distinguish advantages such as high spatiotemporal selectivity and minimal invasiveness [33–35]. The key element in PDT is the photosensitizer which can directly react with the neighboring oxygen to generate $^1O_2$ under the irradiation of a specific laser [36,37]. Subsequently, lethal $^1O_2$ significantly enhanced the intracellular oxidative stress damage, producing many benefits in killing cancer cells. As PDT is able to change the intracellular redox balance *via* producing overwhelming $^1O_2$, it certainly provides a promising strategy to reverse ferroptosis resistance.

Herein, a nanoparticle named BSO-MOF-HA (BMH) consisting of metal organic framework (MOF) and ferroptosis inducer of BSO was developed to reverse the resistance to ferroptosis. MOF with high stability was first constructed by a typical photosensitizer of TCPP and metal ion of Zr6 [38–40]. In order to endow the MOFs with the active targeting to CD44 receptors over-expressed cancer cells, Hyaluronic acid (HA) was used for surface decorate of MOF [41]. BSO was chosen as ferroptosis inducer because 4T1 cells demonstrated resistance to it. Under light irradiation, TCPP in the MOF can convert the light energy into chemical energy, producing $^1O_2$ [42]. BSO in the MOF can inhibit glutamate cysteine ligase (GCL) involved in GSH synthesis pathway, inhibiting the antioxidative defense system [43]. Therefore, the combination of PDT with BSO is expected to produce enhanced oxidative stress damage and therefore trigger ferroptotic cell death. In addition, both ferroptosis and PDT were expected to effectively upregulate the CRT exposure, the HMGB1 release and the ATP secretion, thus inducing the ICD effect and producing the anti-tumor immune effect (Fig. 1) [18,44]. Taken together, combination of oxidative damage and antioxidative defense inhibition would be an effective strategy to reverse ferroptosis resistance in order to take full advantage of ferroptosis in cancer treatment.

2. Material and methods

2.1. Materials

4-hydroxybenzaldehyde was provided by Sigma-Aldrich (Lenexa, USA). Propionic acid and pyrrole were purchased from Macklin (Shanghai, China). Zirconyl chloride octahydrate ($ZrOCl_2·8H_2O$), L-Buthionine-(S, R)-sulfoximine (BSO) and hyaluronic acid (HA) were provided by Aladdin (Shanghai, China). The cell culturing reagents were supplied by Meilun Biotechnology (Dalian, China). All test kits and fluorescent probes used in cell experiments were purchased from Beyotime Biotechnology Co. Ltd (Nantong, China) and Thermo Fisher Scientific, respectively. All the antibodies used in western blotting were offered by Abcam (Cambridge, England). The antibodies using for flow cytometry were offered by Proteintech Group, Inc. (Chicago, USA). The other chemical reagents were analytically pure and provided by Concord Technology Co. Ltd. (Tianjin, China).

4T1 cell line was purchased from Chinese Academy of Sciences. Cells were grown in DMEM medium with 10% FBS and antibiotics (100 U/ml penicillin-streptomycin). The cells were incubated at 37 °C under 5% CO_2.

Female BALB/c mice (5 weeks old, 18–20 g) were purchased from Huafukang Biological Technology Co. Ltd (Beijing, China). The procedures of animal experiments were in compliance with ethics of animal experimentation of Shenyang Pharmaceutical University.

2.2. Synthesis of photosensitizer-TCPP

TCPP was synthesized according to the previous article [45]. In brief, 4-formylbenzoic acid (3.0 g, 0.02 mol) and propionic acid (80.0 ml) were added into a flask and heated to 130 °C. Pyrrole (1.39 ml, 0.02 mol) was added and refluxed for about 1 h. Then methanol (200.0 ml) was added into the flask and leave the flask standing overnight. The purple-
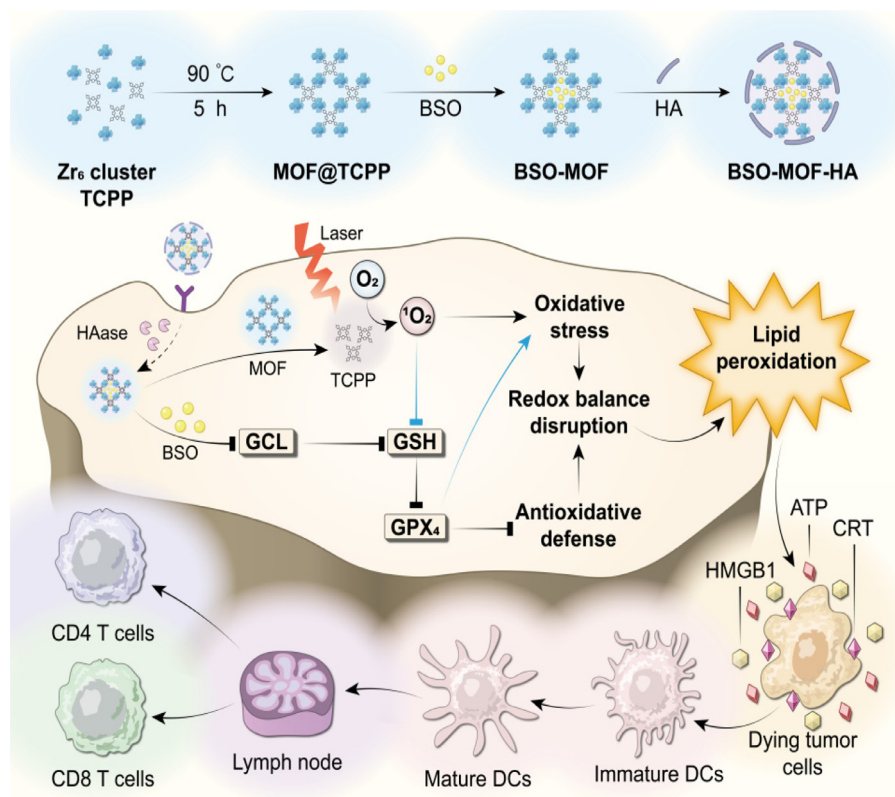
Fig. 1 – Schematic illustration of enhanced ferroptosis of BSO-MOF-HA. Photosensitizer-TCPP produced $^1O_2$ to boost oxidative stress under irradiation. BSO released from BSO-MOF-HA inhibited GCL to block GSH synthesis and inactivate GPX4, leading to compromised antioxidative defense. The combination of TCPP and BSO shifted intracellular redox balance to oxidative stress, resulting in increased lipid peroxidation and ferroptosis. The ferroptotic cancer cells released ATP, HMGB1 and expressed CRT to stimulate immune response through DCs maturation and T lymphocytes activation.

dark precipitation was formed and then refined by adjusting pH with Na_2CO_3 and HCl. The yield rate of TCPP is 52.67%. ^{1}H-NMR spectroscopy (Bruker DRX-600, Germany) and MS (LC-MSD-Trap-SL, Agilent, USA) were used to characterize TCPP.

2.3. Preparation of MOFs

MOF@TCPP (MOF) was obtained according to the previous publication [39]. Briefly, 5.0 ml N, N-dimethylformamide (DMF) containing 30.0 mg $ZrOCl_2 \cdot 8H_2O$ (0.093 mmol) and 0.28 g benzoic acid (2.3 mmol) was heated to 90 °C and stirred for 20 min. Meanwhile, another fresh 5.0 ml DMF solution containing 10.0 mg TCPP (0.013 mmol) was prepared. Then, two DMF solutions were mixed up and stirred at 90 °C for 5 h. MOF was harvested through centrifugation at 12,000 rpm for 30 min and washed with fresh DMF, ethanol and DI water in sequence. Afterwards, 10.0 mg BSO and 10.0 mg MOF were mixed up and stirred for 24 h at 30 °C. BSO-MOF (BM) was also obtained by centrifugation (12,000 rpm, 30 min) and washed by DI water twice to remove the free BSO. In order to prepare MOF-HA (MH) and BSO-MOF-HA (BMH), MOFs (MOF and BM) were further conjugated with hyaluronic acid (HA) by mixing 10.0 mg MOFs with 2.0 mg HA and sonicated for 5 min under ultrasound at 25 °C. Then MH and BMH were washed with DI water twice and collected by centrifugation (12,000 rpm, 30 min).

2.4. Characterizations of MOFs

Transmission electron microscopy (TEM, JEM-1230, Japan) was used to observe the morphology of the MOF complexes. Powder X-ray diffraction spectra (PXRD, Bruker-AXS D8, Germany) was used to characterize the crystal structures of MOF and BMH. Average hydrodynamic size and zeta potentials of MOFs were recorded with dynamic light scattering (DLS, Nikon, Worcestershire, UK). The encapsulation efficiency of BSO in MOFs was measured by centrifugation at 12,000 rpm for 30 min. After centrifugation, the supernatant was discarded to remove the free BSO. The MOF was redispersed in DI water, followed by repeating the procedure twice. The BSO concentration in supernatant solution was measured by HPLC (WondaSil C_{18}, 250 mm × 4.6 mm, 5 µm, Agilent, USA) at 210 nm. The detected condition for HPLC were as follow: methanol:water = 20:80, flow rate = 0.4 ml/min. The encapsulation efficiency (EE) and drug loading (DL) was

calculated according to the following formula.

$$EE\% = \frac{\text{The encapsulated BSO}}{\text{The encapsulated BSO} + \text{The free BSO in the supernant}} \times 100\%$$

$$DL\% = \frac{\text{The amount of added BSO} - \text{The amount of BSO in the superant}}{\text{The weight of MOFs}} \times 100\%$$

2.5. *In vitro release profile of BSO*

BMH (1 mg/ml, 2 ml) in DI water or in hyaluronidase aqueous solution (400–1000 units/mg) was loaded into dialysis bags (3500 Da molecular weight cutoff). The dialysis bags were immersed in 10 ml phosphate buffers (PBS, pH 7.4, pH 6.5 and pH 5.0) with the shaking speed of 100 rpm at 37 °C. At predetermined time points, 1 ml dissolution medium was taken out and 1 ml fresh PBS was added back in order to maintain the volume of release medium. The concentration of BSO in the released medium was measured by HPLC at 210 nm (WondaSil C_{18}, 250 mm × 4.6 mm, 5 μm, Agilent, USA). The cumulative released amount of BSO from the MOF was calculated as follow:

$$D_n = C_n \times 10 + 1 \sum_{i=1}^{n-1} C_i$$

Where, D_n is the cumulative release amount of BSO at the time point of n, C_n is the concentration of BSO in the release medium at time point of n, C_i is the concentration of BSO in the release medium at time point of n-1.

2.6. *Cellular uptake*

In vitro cellular uptake was measured by confocal laser scanning microscopy (CLSM, TCS-SP2, Germany) and flow cytometry (FCM, BD Bioscience, Bedford, MA) respectively. 4T1 cells were inoculated on 6-wells plates (1×10^5 cells/well) and incubated overnight. The supernatant was subsequently discarded and cells were further treated with BMH (TCPP = 20 μg/ml). Meanwhile, cells pre-treated with HA (1 mg/ml) for 1 h were used to study the targeting effect of HA. After cultured for different durations, the cells were fixed with 1 ml pre-cooled paraformaldehyde for 20 min and the nuclei were stained by Hoechst 33258 for 15 min. In addition, 4T1 cells (1×10^5 cells/well) were treated with PBS, MOF, BM and BMH for 6 h, respectively. Then the cells were digested, collected and subjected to FCM test.

2.7. *Cell viability assay*

4T1 cells (1×10^4 cells/well) were seeded into 96-well plates and cultured for 12 h. Then, the cells were incubated with different MOFs at various concentrations (TCPP = 0, 5, 10, 15, 20, 25, 30, 35, 40 μg/ml). After incubation for 6 h, the fresh medium was replaced. The cell with/without irradiation (650 nm, 50 mW/cm^2, 3 min) were further incubated for additional 48 h. Then, 20 μl MTT solution (5 mg/ml) was added and cultured for additional 4 h. Afterwards, the supernatants were replaced with 150 μl DMSO. The absorbance was measured at 570 nm with a microplate reader (M1000 Pro,

Tecan, Switzerland). To study the influence of ferrostatin-1 (Fer-1, ferroptosis inhibitor) or Ac-DEVD-CHO (Apo, apoptosis inhibitor) on the cytotoxicity of MOFs, the cells were pretreated with Fer-1 or Apo for 2 h before addition of different formulations.

2.8. *The intracellular ROS generation and GSH level determination*

The ROS inside the cells was measured by both CLSM and FCM. 4T1 cells were seeded on 6-wells plates (1×10^5 cells/well) and incubated overnight. The supernatant was replaced by the fresh medium containing different MOF formulations and incubated for 6 h. After 10 μM 2′,7′-Dichlorofluoresceindiacetate (DCFH-DA) added and cultured for additional 30 min, the cells were washed and subjected to the laser irradiation (650 nm, 50 mW/cm^2, 30 s). Then, the cells were collected and analyzed by FCM. As for CLSM method, the cell slides were pre-placed into the cells plates before cell seeding. After treated the cells same as FCM method, the cell slides were fixed with 4% formaldehyde and sealed with antifade mounting medium (containing DAPI) to be observed by CLSM. With regard to GSH determination, the cells were seeded and treated same as FCM method used in ROS detection, but the irradiation time was changed to 3 min. Followed by further incubated for 12 h, the content of total GSH and Glutathiol (GSSG) was determined according to standard protocols provided by the manufacturers.

2.9. *GPX4 expression detected by western blotting*

4T1 cells (1×10^5 cells/ml) were treated with formulations, irradiated (650 nm, 50 mW/cm^2) for 1 min and then cultured for additional 48 h. Afterwards, the cells were collected and lysed on ice for 30 min. After quantification with BCA test kits, the total protein was sampled and separated by 12% SDS-PAGE gel. Then the target proteins were transferred onto the poly vinylidene fluoride (PVDF) membrane and blocked with skim milk, followed by soaking in the primary antibodies of β-actin or GPX4 at 4 °C overnight. PVDF membranes were washed for three times with TBST and incubated with horseradish peroxidase-conjugated secondary antibody for 2 h at 25 °C. Enhanced chemiluminescence (ECL) substrate kit was applied to visualize the protein bands.

2.10. *Ferroptosis evaluation induced by MOFs*

Ferroptosis induced by MOFs was detected by mitochondria morphology observation and lipid peroxides (LPO) staining. 4T1 cells were inoculated in 6-well plates at the density of 1×10^5 cells/well and cultured for one night. Then the cells were cultured with PBS, MH and BMH (TCPP = 20 μg/ml) for 6 h respectively, followed by irradiation (650 nm, 50 mW/cm^2, 3 min). Then the cells were further incubated for 6 h. After washed with PBS and incubated with C11-BODIPY581/591 (20 μM, diluted with DMEM) for 30 min, the cells were collected and analyzed by FCM. As for mitochondria morphology observation, the cells were seeded, treated and irradiated same as FCM method, but further incubated

for 12 h. Then, the cells were fixed (2.5% glutaraldehyde) and collected through centrifugation (1000 rpm, 5 min). The cells were further fixed, embedded, sectioned, stained and observed by transmission electron microscope (TEM, HITACHI, HT7700,120 kv).

2.11. In vitro immunogenic cell death effect evaluation

Cells were seeded in 6-well plates (1×10^5 cells/well) and incubated overnight. Then, treated the cells with PBS, MH and BMH (TCPP = 20 μg/ml) for 6 h, respectively. After replacing fresh medium, the cells were further incubated for 24 h. The supernatants collected at 6 h and 24 h were used for ATP and HMGB1 detection according to the standard protocols provided by the manufacturers, respectively. For CRT detection, the cells were blocked with 3% bovine albumin (BSA) for 30 min and incubated with anti-calreticulin antibody at 25 °C for 1 h. The cells were incubated with Goat Anti-Rabbit IgG (fluorescence conjugated) for 40 min followed by testing with FCM. As for CLSM detection, the cell slides were pre-placed in to the cells plates before cell seeding. After treat the cell same as FCM test, but the time for primary and secondary antibody incubation was 12 h at 4 °C and 1 h at 25 °C respectively, the cell slide were taken out and sealed with antifade mounting medium (containing DAPI) to be observed by CLSM.

2.12. MOFs biodistribution study

4T1 cells (1×10^6) were subcutaneously injected into the female BALB/c mice at the right flank. When tumors grew to about 150 mm^3, the mice were randomly divided into 2 groups ($n = 3$). 200 μl MOFs (BM and BMH) were injected (i.v., TCPP:10 mg/kg, BSO:2.5 mg/kg). At 2, 6, 12, 24 and 36 h, the mice were anesthetized and imaged by the Carestream FX PRO Image System (Carestream Health, USA). All the mice were sacrificed at 36 h and excised for tumors and major organs. The organs and tumors were imaged for observation the distribution of BM and BMH.

2.13. In vivo therapeutic efficacy study

The 4T1 tumor-bearing mice was established. The mice were randomly divided into 8 groups ($n = 5$), which were classified as follows: (1) Saline;(2) Saline + laser;(3) MOF;(4) MOF + laser (MOF+);(5) MOF-HA (MH);(6) MOF-HA + laser (MH+);(7) BSO-MOF-HA (BMH);(8) BSO-MOF-HA + laser (BMH+). The mice were treated with different formulations every 3 d (i.v., TCPP:10 mg/kg, BSO:9.6 mg/kg, 3 dosage). For laser irradiation groups, the mice were irradiated (650 nm, 220 Mw/cm^2) for 10 min 24 h after administration. During the experiments, the body weight and tumor volumes (width$^2 \times$ length $\times$ 0.5) were recorded every 2 d. The mice were sacrificed and treated tumors were excised at the 14 th d, tumor tissues and major organs (heart, liver, spleen, lung, and kidney) were collected for HE staining, Ki67 staining, immunofluorescence staining (ROS, CRT and HMGB1) and immunohistochemical staining (GPX4) according to the standard protocols provided by the manufacturers.

2.14. In vivo immune response evaluation induced by MOFs

The bilateral subcutaneous 4T1-bearing model was established by subcutaneously injected 4T1 cells (1×10^6) into mice at the left flank 4 d after primary tumor establishment. The primary tumor received treatments from 7 th d (i.v., TCPP:10 mg/kg, BSO:9.6 mg/kg, every 3 d, 3 dosage). At 2 d after last treatment, all tumors and tumor-draining lymph nodes (TDLNs) were collected and prepared into single cell suspensions via digested by collagenase A and DNAase at 37 °C for 1 h. For labeling activated T cells, tumors tissues were incubated with anti-mouse FITC–CD3, anti-mouse APC–CD4 and anti-mouse PE-CD8 antibodies. For labeling maturated DCs, TDLNs were incubated with anti-mouse PE-CD11c, anti-mouse FITC–CD86 and anti-mouse PECy7-CD80 antibodies. After incubated for 20 min at 25 °C, the cells were washed for twice with PBS solution and detected via FCM.

2.15. Toxicity evaluation (liver and kidney function index)

For safety evaluation, healthy female BALB/c mice were treated with saline, MOF and BMH (i.v., TCPP:10 mg/kg). After 24 h, the serum was collected through centrifugation at 3000 rpm for 30 min. The levels of alanine aminotransferase (ALT), aspartate amino-transferase (AST), blood urea nitrogen (BUN) and uric acid (UA) in the serum were measured with a biochemical analyzer (Chemray 240, Rayto, Shenzhen, China).

2.16. Statistical analysis

All the experiments were carried out at least three times in parallel. The results were presented as mean values $\pm$ standard deviation. Statistical significance was calculated by two-tailed Student's t-test using Grahpad prism 8.0. $*P < 0.05$, $**P < 0.01$, $***P < 0.001$ and $****P < 0.0001$.

3. Results and discussion

3.1. Characterization results of TCPP, MOF, BM, MH and BMH

The δ_H 8.86 (s, 8H) and δ_H 8.37 (dd, 16H) in ^{1}H-NMR spectra represented the specific hydrogens on pyrrole and benzene rings of TCPP respectively (Fig. S1). The m/z 789.5 in mass spectra represented the molecular weight for [M-H]$^-$ of TCPP (Fig. S2). These results indicated the successful synthesis of TCPP. MOF prepared from metal Zr6 and TCPP was firstly characterized by UV and fluorescence scanning spectrometry (Fig. 2A and 2B). TCPP exhibited no obvious UV absorption and fluorescence emission curves in PBS due to its poor aqueous solubility. However, MOF in PBS exhibited similar UV absorption curve and fluorescence emission profiles with those of TCPP in DMF, indicating that TCPP was solubilized in the MOF. Besides, BMH revealed similar PXRD pattern and color appearance under laser with MOF (Figs. S3 and S4), indicating that BSO encapsulation and surface modification with HA had no influence on the structure of MOF and the
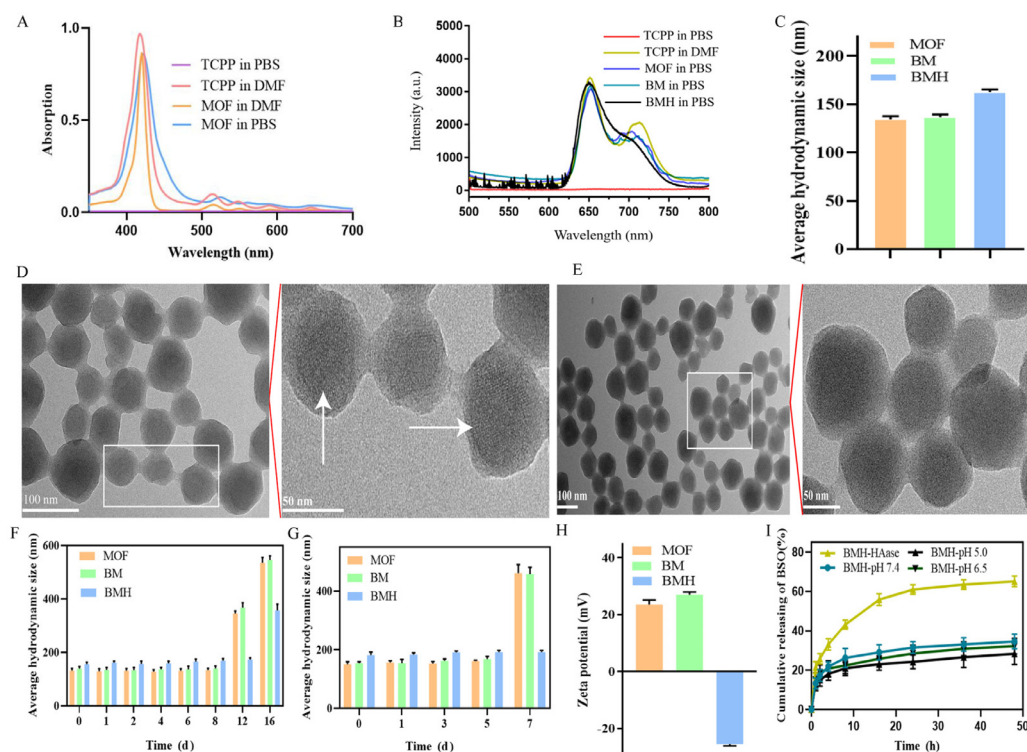
Fig. 2 – Characteristics of the different MOFs. (A) The UV–Vis spectra of TCPP and MOF in different solvents. (B) The fluorescence emission spectrums of TCPP, MOF, BM and BMH in different solvents. (C) The average hydrodynamic size of MOF, BM and BMH (PDI for MOF:0.105, PDI for BM:0.055, PDI for BMH:0.146). (D) The typical image of MOF detected by TEM. (E) The typical image of BMH detected by TEM. (F) The average hydrodynamic sizes of MOF, BM and BMH in PBS medium at different time points. (G) The average hydrodynamic sizes of MOF, BM and BMH in 10% FBS containing medium. (H) The average zeta potentials of MOF, BM and BMH. (I) The cumulative release of BSO from BMH in different releasing mediums.

physical properties of TCPP. The calculated encapsulation and loading efficiency of BSO were 95.60% and 79.08%.

MOF showed an average hydrodynamic diameter of 138.3 nm and 136.6 nm before and after incorporation BSO respectively. Surface modification of MOF with HA slightly increased the average hydrodynamic size to about 162.5 nm (Fig. 2C). TEM was used to observe the morphology of MOF and BMH (Fig. 2D and 2E). MOF exhibited spherical shape with visible mesoporous channel structure which disappeared in BMH due to HA decoration. MOF showed little variation in average hydrodynamic size in PBS medium for 8 d and in culture medium containing 10% FBS for 5 d, respectively (Fig. 2F and 2G). It's worth to note that HA decoration further enhanced the stability of MOF as it extended the unchanged particle size period to 12 d in PBS medium and to 7 d in culture medium containing 10% FBS, respectively. The average zeta potential value of MOF was 26.1 mV and the incorporation of BSO had little effect on the zeta potential (28.2 mV). The zeta potential of MOF with HA surface decoration decreased to about −25.5 mV (Fig. 2H), indicating the successful coverage of negative HA molecules on the surface of MOFs. The drug release profiles of BMH were shown in Fig. 2I. BMH showed similar BSO release profiles in PBS from pH 5.0 to pH 7.4 and incomplete BSO release over 48 h with acumulative percentage release range from 28.39% to 34.59%. However, the BSO release amount was significantly improved to 65.34% when HAase

was added to degrade HA. These results demonstrated that HA served as a protection layer to slow down the BSO release from the MOF. It could be expected that HA decoration can reduce the premature drug leakage during blood circulation but produce rapid BSO release in the HAase rich tumor microenvironment.

3.2. Reversing ferroptosis resistance in 4T1 cells

Cellular uptake of BMH was investigated by CLSM and FCM respectively. As shown in Fig. 3A, BMH showed a typical time-dependent TCPP accumulation. The red fluorescence of TCPP increased with time and reached maximum at 6 h. The red fluorescence intensity significantly decreased when HA (1 mg/ml) was used to pre-saturate the receptors of cancer cells, indicating the positive role of HA in cellular uptake. Because HA has strong affinity to CD44 receptor, which is over-expressed on some cancer cells [46–48], HA-modified MOF nanoparticles imparted active targeting delivery of the payload. FCM results were consistent with CLSM observation (Fig. 3B). Despite the efficient cellular uptake, both MH and BMH solution displayed negligible cytotoxicity against 4T1 cells (Fig. 3C), demonstrating the resistance of 4T1 cancer cells to BSO induced ferroptosis. Under laser irradiation, both BMH+ and MH+ exhibited remarkably increased cytotoxicity against 4T1 cells (Fig. 3D, *P> 0.05). The cell viability of MH+ and BMH+ decreased from 94.40% (without laser) to 29.90%
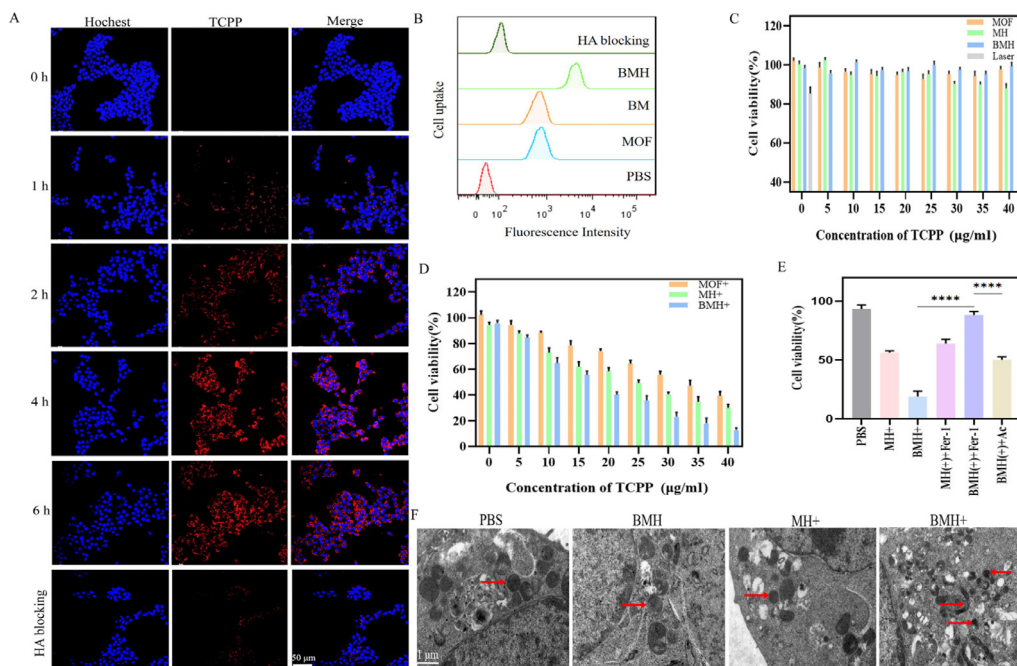
Fig. 3 – Cellular uptake, *in vitro* cytotoxicity of different MOFs and TEM images of mitochondria. (A) Cellular uptake behavior of BMH at various conditions detected by CLSM (scale bar = 50 μm). (B) Cellular uptake of BMH after 6 h treatment detected by FCM. (C) *In vitro* cytotoxicity of MOFs without irradiation. (D) *In vitro* cytotoxicity of MOFs under irradiation (650 nm, 50 mW/cm^2, 3 min). (E) *In vitro* cytotoxicity of MOFs in presence of ferroptosis inhibitor and apoptosis inhibitor. (F) The images of the mitochondria morphology of the cells after treated with MOFs for 12 h (scale bar = 1 μm).

(with laser) and from 95.80% (without laser) to 12.70% (with laser) respectively (*P < 0.05). The stronger cytotoxicity of BMH$^+$ than MH$^+$ proved that BSO contributed to the cell death under laser irradiation.

To investigate the cell death pathway of BMH+ treated cells, ferroptosis inhibitor-Fer-1 and apotosis inhibitor-Apo were used to investigate the cell death pathway in BMH+ treated group. As shown in Fig. 3E, cell death in BMH+ group was alleviated by the addition of Fer-1 and Apo respectively, suggesting the hybrid cell death pathway of apoptosis and ferroptosis. As compared to Apo that showed 30.66% increase in cell viability, Fer-1 produced 68.66% increase in cell viability. Meanwhile, BMH+ treated cells exhibited dramatic mitochondria morphology change with volume reduction (Fig. 3F), which was usually associated with ferroptosis [49]. These results indicated ferroptosis was the dominant cell death pathway in BMH+ treated cells. In summary, PDT was found to significantly enhance BSO induced ferroptosis in ferroptosis resistant 4T1 cells.

To elucidate the mechanism of the enhanced ferroptosis by PDT, cellular ROS, GSH and GPX4 responsible for maintaining the intracellular redox homeostasis were further tested. BMH treated cancer cells exhibited little effect on the intracellular ROS and GSH levels (Fig.4A-4C). To counteract the BSO induced GSH synthesis inhibition, cancer cells have been found to develop TXN pathway and upregulate CD44 variant 9 (CD44v9) expression in order to enhance cystine uptake under the GSH depletion condition [26,29]. The presence of supplementary GSH synthesis and several ROS elimination

pathways to maintain the redox balance also explained the ferroptosis resistance of 4T1 cells to BSO. In contrast to BMH treated cells, both BMH+ and MH+ treated cells exhibited remarkable green fluorescence in Fig.4A, indicating the excessive intracellular ROS generation under irradiation. Moreover, BMH+ treated cells revealed much broader and intenser green fluorescence than MH+. FCM results also confirmed that BMH+ produced higher ROS than MH+ (Fig. 4B). Moreover, it was noteworthy that BMH+ treated cells exhibited remarkably lower intracellular GSH and GPX4 expression levels than MH+ (Fig. 4C and 4D). This proved that ROS generated by TCPP consumed the intracellular GSH, more importantly, further potentiate the activity of BSO in depletion of GSH and the inhibition of GPX4. The synergistic effect of BSO in inhibition of anti-oxidative capacity and TCPP in boosting ROS generation shifted the redox balance towards oxidative stress. Consequently, BMH+ produced more lipid peroxides (LPO) than MH+ (Fig. 4E), leading to the enhanced ferroptosis. In order to investigate the possible immunogenic cell death effect induced by MH+ and BMH+, the DAMPs such as CRT expression, ATP and HMGB1 releasing were detected in sequence. In the fluorescence pictures of CRT, the blue fluorescence indicated for nucleus while the green fluorescence represented for the expressed CRT. Therefore, it was obviously that both MH+ and BMH+ significantly increased the levels of CRT expression, ATP and HMGB1 releasing (Fig. 4F-4J). BMH+ exhibited higher levels of CRT expression, ATP and HMGB1 releasing than MH+ group, indicating the hybrid cell death form in which ferroptosis
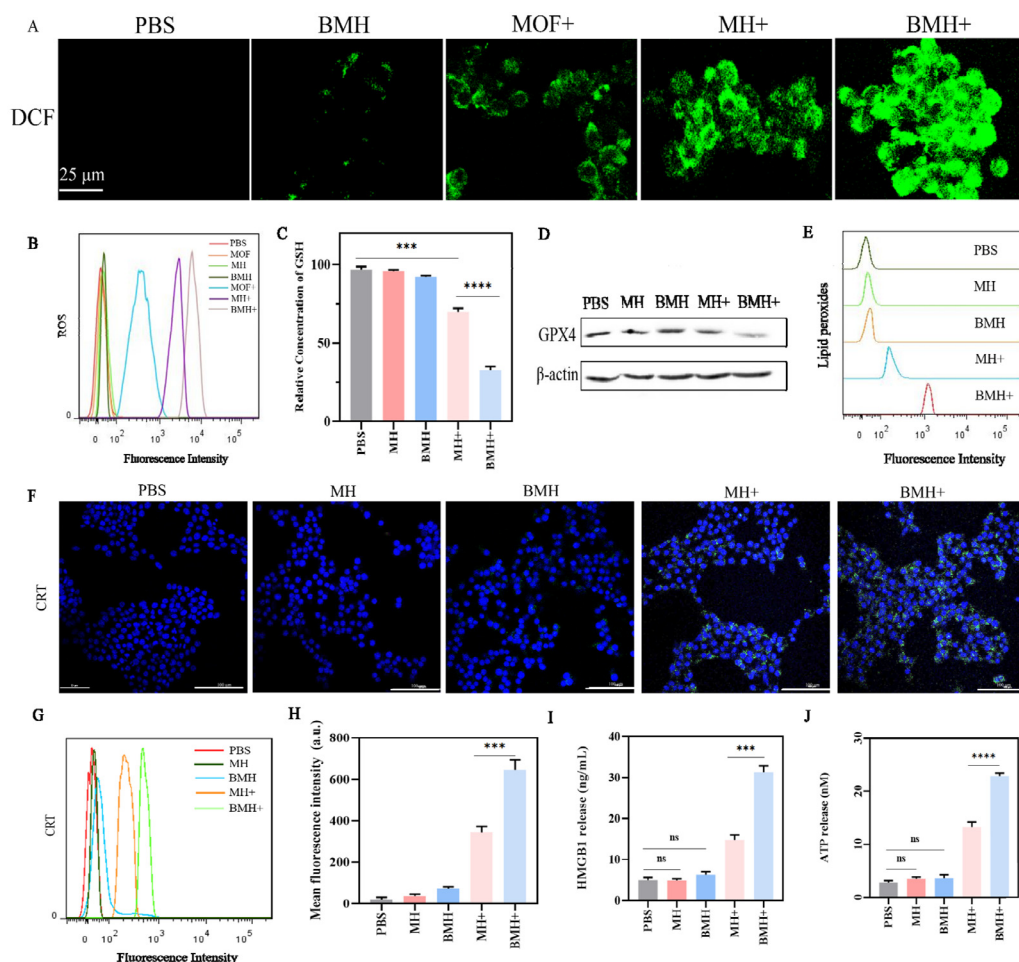
Fig. 4 – The mechanism of reversing ferroptosis resistance in 4T1 cells and the quantification of DAMPs releasing. (A) CLSM detection of intracellular ROS production after treated MOFs with or without irradiation (scale bar: 25 µm). (B) FCM detection of intracellular ROS production after treated MOFs with or without irradiation. (C) Quantification of intracellular GSH levels after treatment with MOFs for 12 h. (D) Quantification of GPX4 expression level after treatment with MOFs for 48 h. (E) Detection of LPO production in cell membranes after treatment with MOFs for 6 h. (F) CLSM detection for CRT exposure after treatment with MOFs for 24 h (scale bar: 100 µm). (G) FCM detection for CRT exposure after treatment with MOFs for 24 h. (H) The mean fluorescence intensity of CRT expression ($n = 3$, ***$P < 0.001$) (I) HMGB1 releasing quantification after treatment with MOFs for 24 h. (J) ATP releasing quantification after treatment with MOFs for 6 h ($n = 3$, ***$P < 0.001$, ****$P < 0.0001$).

dominated produced much stronger ICD effect than PDT induced apoptosis.

3.3. The biodistribution, anti-tumor effect and safety evaluation of MOFs

The distribution of MOFs (BM and BMH) in the 4T1 tumor bearing mice was studied with TCPP as an indicator. BMH exhibited a typical time-dependent accumulation profile in the tumor and the maximum fluorescence signal was observed at 24 h after *i.v.* injection (Fig 5A). In addition, BMH exhibited much stronger fluorescence signal in tumor tissue and much less fluorescence signal in the liver than BM. The distribution difference between BMH and BM could be attributed to the HA surface modification, which help to reduce the RES uptake and increase the tumor targeting of the MOF.

To evaluate the anti-tumor effect, different MOF preparations were administered to the 4T1 tumor bearing mice. As expected, BMH showed little tumor growth suppression in the absence of laser irradiation. This also confirmed the ferroptosis resistance of 4T1 tumor to BSO. Under irradiation, the BMH+ treated group showed significantly stronger tumor growth inhibition than MH+ and BMH (Figs. 5B and S5). The results of H&E staining and Ki67 staining revealed more serious necrosis in BMH+ treated tumors than MH+ and BMH treated ones (Fig. 5C and 5D). This confirmed the enhanced anti-tumor effect of co-administration of BSO with TCPP under the laser irradiation. The ROS level and GPX4 expression were further measured to validate the ferroptotic pathway in BMH+ group. As depicted in the Fig.5E, BMH+ produced significant higher ROS level than MH+, BMH and MH in the tumor. This could be attributed to the synergistic effect of PDT in producing ROS and BSO
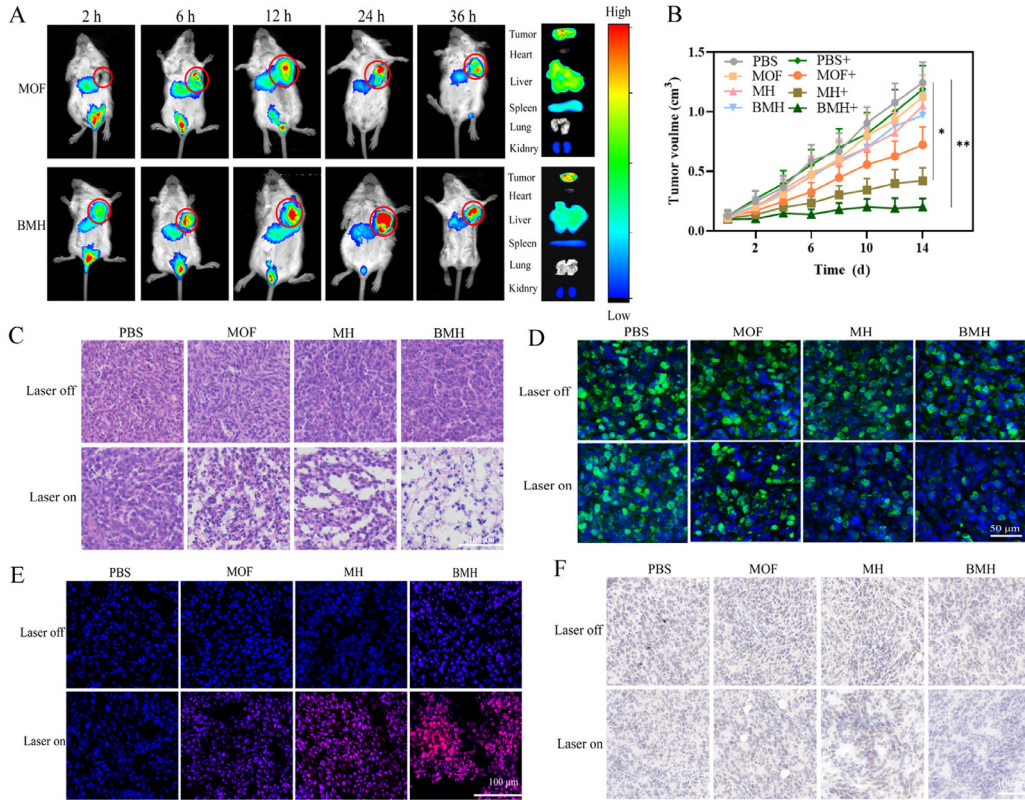
Fig. 5 – The biodistribution and anti-tumor effect evaluation of MOFs. (A) *In vivo* fluorescence images of BALB/c mice bearing 4T1 tumor at 2 h, 6 h, 12 h, 24 h and 36 h post injection of BM and BMH and *Ex-vivo* fluorescence of major organs and tumors after treatment for 36 h. (B) The primary tumor growth curve during 14 d treatment (n = 5, *P < 0.05, **P < 0.01). (C) The H&E staining result of primary tumors after treatment with MOFs (scale bar=100 μm). (D) The Ki67 expression of primary tumors after treatment with MOFs (scale bar=50 μm). (E) The ROS generation *in vivo* after treatment with MOFs (scale bar=100 μm). (F) The GPX4 expression *in vivo* after treatment with MOFs (scale bar=100 μm).
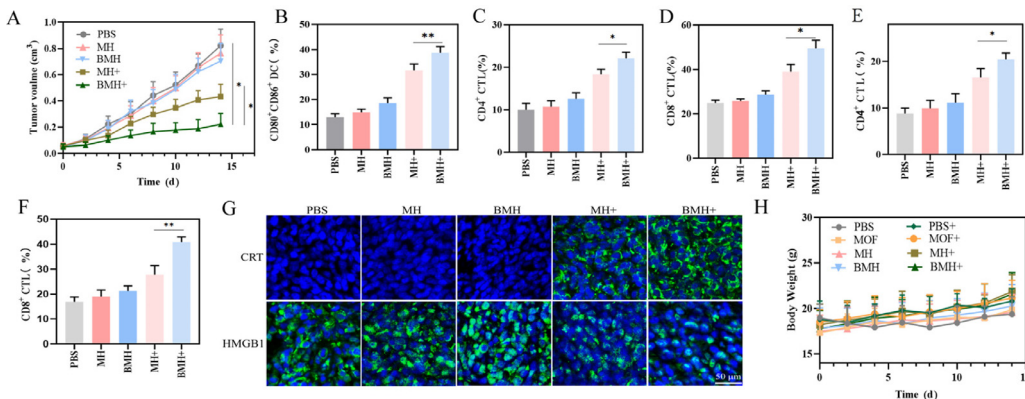
Fig. 6 – *In vivo* ICD effect evaluation and the safety evaluation of MOFs. (A) The distant tumor growth curves of 4T1 tumor-bearing mice during the treatment. (B) Quantification of maturated DCs in primary TDLNs by FCM. (C) Quantification of cytotoxic T lymphocytes (CD3+CD4+) in primary tumors by FCM. (D) Quantification of cytotoxic T lymphocytes (CD3+CD8+) in primary tumors by FCM. (E) Quantification of cytotoxic T lymphocytes (CD3+CD4+) in distant tumors by FCM. (F) Quantification of cytotoxic T lymphocytes (CD3+CD8+) in distant tumors by FCM. (G) The CRT and HMGB1 expression in the different primary tumors after MOFs treatment. (H) Body weight change of 4T1 tumor-bearing mice during the treatment. (n = 5, *P < 0.05, **P < 0.01).

in inhibiting GSH synthesis. Because GPX4 is a key enzyme inhibiting ferroptosis, the intracellular GPX4 expression was further detected with IHC method. As shown in Fig. 5F, the brown staining representing GPX4 expression was almost completely depleted in BMH+ treated tumors, indicating that BMH+ produced ferroptotic cell death *in vivo*.

To validate the ICD effect *in vivo*, the growth curves of distant tumors, DAMPs release and immune cell levels inside the tumors and TDLNs were further measured. The tumor growth curves and the tumor photos demonstrated that both MH+ and BMH+ groups showed effective distant tumor suppression, indicating the possible ICD effect of the two MOFs (Figs. 6A and S6). Compared to MH and BMH, MH+ significantly increased the proportions of maturated DCs, activated CD4$^+$T cells and CD8$^+$T cells (Fig. 6B-6F). This could be attributed to the positive effect of PDT in boosting the anti-tumor immunity. It was noteworthy that BMH+ displayed much higher CRT level and lower HMGB1 level (Fig. 6G). The more efficient endogenous immunogenic molecules release from ferroptosis certainly produced higher proportions of maturated DCs, activated CD4$^+$T cells and CD8$^+$T cells than MH+ (**$P < 0.01$). This also explained the stronger growth inhibition of BMH+ than MH+. Collectively, the above results elucidated that BMH+ induced ferroptosis could stimulate more potent anti-tumor immunity than PDT.

To evaluated the biocompatibility of MOFs, body weight, biochemical indicators and H&E staining of major organs were recorded. The body weights of mice over 14 d treatment with different MOFs showed no significant variation with PBS (Fig. 6H). Compared to the PBS group, the MOFs (MOF and BMH) treated mice showed negligible variation in the biochemical indicators (ALT, AST, BUN and UA) (Fig. S10). Moreover, H&E staining of major organs after 14 d treatment revealed on obvious histological damage in each MOF-treated group (Fig. S11). Collectively, these results indicated the safety and biocompatibility of MOFs.

4.   Conclusion

In summary, the HA surface decorated MOFs was constructed by the photosensitizer of TCPP and the metal ion of Zr6 and used to incorporate ferroptosis inducer of BSO. The BSO incorporated MOF showed nanosized particle, high stability and encapsulation efficiency. HA surface decoration reduced premature leak of BSO by decreasing its release from the MOF and imparted active targeting by interacting with CD44 receptors. The MOFs were found to remarkably increase the intracellular ROS level under irradiation, enhancing the oxidative stress. The excessive ROS was found to change the intracellular redox balance and potentiate the BSO induced GSH depletion, GPX4 inactivation and LPO accumulation, leading to synergistic effect and effective ferroptotic cell death. Ferroptosis was also found to induce adequate DAMPs (CRT, ATP and HMGB1) releasing and dramatically raised the proportions of maturated DCs and activated cytotoxic T lymphocytes (CD4+ and CD8+ T cells), leading to the boosted anti-tumor immunity. Therefore, manipulation of intracellular redox homeostasis by MOFs integrating PDT and

GSH inhibitor has been demonstrated as an effective strategy to overcome ferroptosis resistance.

Supplementary materials

Supplementary material associated with this article can be found, in the online version, at doi:10.1016/j.ajps.2022.11.004.

REFERENCES

[1] Dixon SJ, Lemberg KM, Lamprecht MR, Skouta R, Zaitsev EM, Gleason CE, et al. Ferroptosis: an iron-dependent form of nonapoptotic cell death. Cell 2012;149(5):1060–72.

[2] Yu X, Shang T, Zheng G, Yang H, Li Y, Cai Y, et al. Metal-polyphenol-coordinated nanomedicines for Fe(II) catalyzed photoacoustic-imaging guided mild hyperthermia-assisted ferroustherapy against breast cancer. Chin Chem Lett 2022;33(4):1895–900.

[3] Wang S, Liao H, Li F, Ling D. A mini-review and perspective on ferroptosis-inducing strategies in cancer therapy. Chin Chem Lett 2019;30(4):847–52.

[4] An P, Gao Z, Sun K, Gu D, Wu H, You C, et al. Photothermal-enhanced inactivation of glutathione peroxidase for ferroptosis sensitized by an autophagy promotor. ACS Appl Mater Interfaces 2019;11(46):42988–42997.

[5] Chen X, Kang R, Kroemer G, Tang D. Broadening horizons: the role of ferroptosis in cancer. Nat Rev Clin Oncol 2021;18(5):280–96.

[6] Xu T, Ma Y, Yuan Q, Hu H, Hu X, Qian Z, et al. Enhanced ferroptosis by oxygen-boosted phototherapy based on a 2-in-1 nanoplatform of ferrous hemoglobin for tumor synergistic therapy. ACS Nano 2020;14(3):3414–25.

[7] Tang H, Li C, Zhang Y, Zheng H, Cheng Y, Zhu J, et al. Targeted manganese doped silica nano GSH-cleaner for treatment of liver cancer by destroying the intracellular redox homeostasis. Theranostics 2020;10(21):9865–87.

[8] Stockwell BR, Friedmann Angeli JP, Bayir H, Bush AI, Conrad M, Dixon SJ, et al. Ferroptosis: a regulated cell death nexus linking metabolism, redox biology, and disease. Cell 2017;171(2):273–85.

[9] Shi Z, Naowarojna N, Pan Z, Zou Y. Multifaceted mechanisms mediating cystine starvation-induced ferroptosis. Nat Commun 2021;12(1):4792.

[10] Li J, Meng X, Deng J, Lu D, Zhang X, Chen Y, et al. Multifunctional micelles dually responsive to hypoxia and singlet oxygen: enhanced photodynamic therapy via interactively triggered photosensitizer delivery. ACS Appl Mater Interfaces 2018;10(20):17117–28.

[11] Liang C, Zhang X, Yang M, Dong X. Recent progress in ferroptosis inducers for cancer therapy. Adv Mater 2019;31(51):e1904197.

[12] Liang X, Chen M, Bhattarai P, Hameed S, Tang Y, Dai Z. Complementing cancer photodynamic therapy with ferroptosis through iron oxide loaded porphyrin-grafted lipid nanoparticles. ACS Nano 2021;15(12):20164–80.

[13] Sun F, Peng Y, Li Y, Xu M, Cai T. Fenton-reaction-triggered metabolism of acetaminophen for enhanced cancer therapy. Chin Chem Lett 2022.

[14] Lei G, Zhuang L, Gan B. Targeting ferroptosis as a vulnerability in cancer. Nat Rev Cancer 2022.

[15] Efimova I, Catanzaro E, Van der Meeren L, Turubanova VD, Hammad H, Mishchenko TA, et al. Vaccination with early ferroptotic cancer cells induces efficient antitumor immunity. J Immunother Cancer 2020;8(2).

[16] Yu B, Choi B, Li W, Kim DH. Magnetic field boosted ferroptosis-like cell death and responsive MRI using hybrid vesicles for cancer immunotherapy. Nat Commun 2020;11(1):3637.

[17] Turubanova VD, Balalaeva IV, Mishchenko TA, Catanzaro E, Alzeibak R, Peskova NN, et al. Immunogenic cell death induced by a new photodynamic therapy based on photosens and photodithazine. J Immunother Cancer 2019;7(1):350.

[18] Chen Z, Liu L, Liang R, Luo Z, He H, Wu Z, et al. Bioinspired hybrid protein oxygen nanocarrier amplified photodynamic therapy for eliciting anti-tumor immunity and abscopal effect. ACS Nano 2018;12(8):8633–45.

[19] Banstola A, Poudel K, Kim JO, Jeong JH, Yook S. Recent progress in stimuli-responsive nanosystems for inducing immunogenic cell death. J Control Release 2021;337:505–20.

[20] Zhang S, Wang J, Kong Z, Sun X, He Z, Sun B, et al. Emerging photodynamic nanotherapeutics for inducing immunogenic cell death and potentiating cancer immunotherapy. Biomaterials 2022;282:121433.

[21] Wang W, Green M, Choi JE, Gijon M, Kennedy PD, Johnson JK, et al. CD8(+) T cells regulate tumour ferroptosis during cancer immunotherapy. Nature 2019;569(7755):270–4.

[22] Kishton RJ, Sukumar M, Restifo NP. Metabolic regulation of T cell longevity and function in tumor immunotherapy. Cell Metab 2017;26(1):94–109.

[23] Chen G, Zhang H, Wang H, Wang F. Immune tolerance induced by immune-homeostatic particles. Eng Regener 2021;2:133–6.

[24] Zheng DW, Lei Q, Zhu JY, Fan JX, Li CX, Li C, et al. Switching apoptosis to ferroptosis: metal-organic network for high-efficiency anticancer therapy. Nano Lett 2017;17(1):284–91.

[25] Ma Q. Role of nrf2 in oxidative stress and toxicity. Annu Rev Pharmacol Toxicol 2013;53:401–26.

[26] Suzuki T, Motohashi H, Yamamoto M. Toward clinical application of the Keap1-Nrf2 pathway. Trends Pharmacol Sci 2013;34(6):340–6.

[27] Ishimoto T, Nagano O, Yae T, Tamada M, Motohara T, Oshima H, et al. CD44 variant regulates redox status in cancer cells by stabilizing the xCT subunit of system xc(-) and thereby promotes tumor growth. Cancer Cell 2011;19(3):387–400.

[28] Jogo T, Oki E, Nakanishi R, Ando K, Nakashima Y, Kimura Y, et al. Expression of CD44 variant 9 induces chemoresistance of gastric cancer by controlling intracellular reactive oxygen spices accumulation. Gastric Cancer 2021;24(5):1089–99.

[29] Zheng J, Conrad M. The Metabolic Underpinnings of Ferroptosis. Cell Metab 2020;32(6):920–37.

[30] Hayano M, Yang WS, Corn CK, Pagano NC, Stockwell BR. Loss of cysteinyl-tRNA synthetase (CARS) induces the transsulfuration pathway and inhibits ferroptosis induced by cystine deprivation. Cell Death Differ 2016;23(2):270–8.

[31] Gao J, Luo T, Wang J. Gene interfered-ferroptosis therapy for cancers. Nat Commun 2021;12(1):5311.

[32] Song X, Liu J, Kuang F, Chen X, Zeh HJ 3rd, Kang R, et al. PDK4 dictates metabolic resistance to ferroptosis by suppressing pyruvate oxidation and fatty acid synthesis. Cell Rep 2021;34(8):108767.

[33] Wu N, Tu Y, Fan G, Ding J, Luo J, Wang W, et al. Enhanced photodynamic therapy/photothermo therapy for nasopharyngeal carcinoma via a tumour microenvironment-responsive self-oxygenated drug delivery system. Asian J Pharm Sci 2022;17(2):253–67.

[34] Zhou Z, Zhang L, Zhang Z, Liu Z. Advances in photosensitizer-related design for photodynamic therapy. Asian J Pharm Sci 2021;16(6):668–86.

[35] Schlachter A, Asselin P, Harvey PD. Porphyrin-containing MOFs and COFs as heterogeneous photosensitizers for singlet oxygen-based antimicrobial nanodevices. ACS Appl Mater Interfaces 2021;13(23):26651–72.

[36] Yang L, Gao P, Huang Y, Lu X, Chang Q, Pan W, et al. Boosting the photodynamic therapy efficiency with a mitochondria-targeted nanophotosensitizer. Chin Chem Lett 2019;30(6):1293–6.

[37] Wu Y, Li J, Zhong X, Shi J, Cheng Y, He C, et al. A pH-sensitive supramolecular nanosystem with chlorin e6 and triptolide co-delivery for chemo-photodynamic combination therapy. Asian J Pharm Sci 2022;17(2):206–18.

[38] Kim K, Lee S, Jin E, Palanikumar L, Lee JH, Kim JC, et al. MOFx biopolymer: collaborative combination of metal-organic framework and biopolymer for advanced anticancer therapy. ACS Appl Mater Interfaces 2019;11(31):27512–20.

[39] Li SY, Cheng H, Qiu WX, Zhang L, Wan SS, Zeng JY, et al. Cancer cell membrane-coated biomimetic platform for tumor targeted photodynamic therapy and hypoxia-amplified bioreductive therapy. Biomaterials 2017;142:149–61.

[40] Qin Y, Wan Y, Guo J, Zhao M. Two-dimensional metal-organic framework nanosheet composites: preparations and applications. Chin Chem Lett 2022;33(2):693–702.

[41] Yang C, Yu Y, Wang X, Wang Q. Shang L Cellular fluidic-based vascular networks for tissue engineering. Eng Regener 2021;2:171–4.

[42] Cai L, Xu D, Chen H, Wang L, Zhao Y. Designing bioactive micro-/nanomotors for engineered regeneration. Eng Regener 2021;2:109–15.

[43] Niu B, Liao K, Zhou Y, Wen T, Quan G, Pan X, et al. Application of glutathione depletion in cancer therapy: enhanced ROS-based therapy, ferroptosis, and chemotherapy. Biomaterials 2021;277:121110.

[44] Wang Z, Chen L, Ma Y, Li X, Hu A, Wang H, et al. Peptide vaccine-conjugated mesoporous carriers synergize with immunogenic cell death and PD-L1 blockade for amplified immunotherapy of metastatic spinal. J Nanobiotechnol 2021;19(1):243.

[45] Yan GP, Bischa D, Bottle SE. Synthesis and properties of novel porphyrin spin probes containing isoindoline nitroxides. Free Radic Biol Med 2007;43(1):111–16.

[46] Cheng D, Ji Y, Wang B, Wang Y, Tang Y, Fu Y, et al. Dual-responsive nanohybrid based on degradable silica-coated gold nanorods for triple-combination therapy for breast cancer. Acta Biomater 2021;128:435–46.

[47] Du X, Yin S, Wang Y, Gu X, Wang G, Li J. Hyaluronic acid-functionalized half-generation of sectorial dendrimers for anticancer drug delivery and enhanced biocompatibility. Carbohydr Polym 2018;202:513–22.

[48] Ashrafizadeh M, Mirzaei S, Gholami MH, Hashemi F, Zabolian A, Raei M, et al. Hyaluronic acid-based nanoplatforms for Doxorubicin: a review of stimuli-responsive carriers, co-delivery and resistance suppression. Carbohydr Polym 2021;272:118491.

[49] Yagoda N, von Rechenberg M, Zaganjor E, Bauer AJ, Yang WS, Fridman DJ, et al. RAS-RAF-MEK-dependent oxidative cell death involving voltage-dependent anion channels. Nature 2007;447(7146):864–8.